Influence of the sudden stratospheric warming on quasi-2 day waves

Sheng-Yang Gu[1, 2*], Han-Li Liu[3], Xiankang Dou[1, 2], Tao Li[1, 2]

[1]CAS Key Laboratory of Geospace Environment, Department of Geophysics and Planetary Science, University of Science and Technology of China, Hefei, Anhui, China

[2]Mengcheng National Geophysical Observatory, School of Earth and Space Sciences, University of Science and Technology of China, Hefei, Anhui, China

[3]High Altitude Observatory, National Center for Atmospheric Research, Boulder, Colorado, USA

*Corresponding author: S.-Y. Gu, CAS Key Laboratory of Geospace Environment, School of Earth and Space Science, University of Science and Technology of China, 96 Jin-zhai Rd, Hefei, Anhui 230026, China. (gsy@ustc.edu.cn).

Abstract:

The influence of the sudden stratospheric warming (SSW) on quasi-2 day wave (QTDW) with westward zonal wavenumber 3 (W3) is investigated using the Thermosphere-Ionosphere-Mesosphere-Electrodynamics General Circulation Model (TIME-GCM). The summer easterly jet below 90 km is strengthened during an SSW, which results in a larger refractive index and thus more favorable condition for the propagation of W3. In the winter hemisphere, the Eliassen Palm (EP) flux diagnostics indicate that the strong instabilities at middle and high latitudes in the mesopause region are important for the amplification of W3, which are weakened during SSW periods due to the deceleration or even reversal of the winter westerly winds. Nonlinear interactions between the W3 and the wavenumber 1 stationary planetary wave produce QTDW with westward zonal wavenumber 2 (W2). The meridional wind perturbations of the W2 peak in the equatorial region, while the zonal wind and temperature components maximize at middle latitudes. The EP flux diagnostics indicate that the W2 is capable of propagating upward in both winter and summer hemispheres, whereas the propagation of W3 is mostly confined to the summer hemisphere. This characteristic is likely due to the fact that the phase speed of W2 is larger, and therefore its waveguide has a broader latitudinal extension. The larger phase speed also makes W2 less vulnerable to dissipation and critical layer filtering by the background wind when propagating upward.

1. Introduction

The westward quasi-2 day wave (QTDW) is a predominant phenomenon in the mesosphere and lower thermosphere (MLT) region in the summer hemisphere with zonal wavenumbers 2, 3, and 4. The QTDW was observed by the neutral temperature measurements from Upper Atmosphere Research Satellite (UARS) [*Wu et al.*, 1996], Aura satellite [*Tunbridge et al.*, 2011] and Thermosphere Ionosphere and Mesosphere Electric Dynamics (TIMED) satellite [*Gu et al.*, 2013a], and the neutral wind measurements from UARS High Resolution Doppler Imager (HRDI) [*Wu et al.*, 1993], TIMED TIDI [*Gu et al.*, 2013a], and medium frequency radar [*Gu et al.*, 2013b]. In addition, numerical simulations, including one-dimensional model [*Plumb*, 1983], two-dimensinoal model [*Rojas and Norton*, 2007], three dimensional Thermosphere-Ionosphere-Mesosphere-Electrodynamics General Circulation Model (TIME-GCM) [*Yue et al.*, 2012] and the Navy Operational Global Atmospheric Prediction System Advanced Level Physics, High Altitude (NOGAPS-ALPHA) forecast-assimilation system [*McCormack*, 2009], have also been utilized to study the QTDW. Using neutral temperature and horizontal wind observations from the TIMED satellite, *Gu et al.* [2013a] showed that the QTDW with westward zonal wavenumber 3 (W3) is amplified during January/February in the southern hemisphere, and that the QTDW with westward zonal wavenumber 4 (W4) reaches a maximum amplitude during July/August in the northern hemisphere. The amplitude of the W3 is nearly twice as strong as the W4. It is proposed that the W3 is the Rossby-gravity mode (3, 0) [*Salby*, 1981], which can be modulated by the mean flow instabilities [*Plumb*, 1983;

Limpasuvan et al., 2000; *Salby and Callaghan*, 2001; *Yue et al.*, 2012]. Besides, *Limpasuvan et al*. [2000] found that the inertial instability in the equatorial region could also play a role in amplifying QTDW. Nevertheless, the TIME-GCM experiments performed by *Liu et al.* [2004] showed no clear evidence of QTDW amplification around inertial unstable regions, which only causes additional spatial variability. The W4 is first reported by *Rodgers and Prata* [1981] in the radiance data from the Nimbus 6 satellite, which was also confirmed by *Plumb* [1983] with a one-dimensional model under summer easterly conditions. Usually, the W4 is believed to be an unstable mode induced by the summer easterly instabilities [*Plumb*, 1983; *Burks and Leovy*, 1986]. Compared with W3 and W4, there are much less reports on the QTDW with westward zonal wavenumber 2 (W2).

Tunbridge et al. [2011] studied the zonal wavenumbers of the summer time QTDW with satellite temperature observations from 2004 to 2009. They found that the W2 is amplified mainly during January in the southern hemisphere with a maximum amplitude at middle latitudes, which always coincides with the temporal variations of the W3. The horizontal wind observations from the HRDI instrument onboard the UARS satellite showed that the meridional wind perturbations of the W2 maximize in the equatorial region at the mesopause [*Riggin et al.*, 2004]. This W2 was suggested to be excited in-situ at high altitude, which has little direct connection with the 2-day activities at lower altitudes. Anomalous 2-day wave activities with zonal wavenumber 2 were also observed in the Aura/MLS temperature and line-of-sight wind [*Limpasuvan and Wu*; 2009], which was suggested to be an unstable mode induced by the strong summer easterly jet during January 2006. *Rojas and Norton* [2007] found a wavenumber 2 westward propagating wave mode with a period of 49 h in a linear two-dimensional model under boreal summer easterly condition, which maximized at middle and high latitudes in the summer hemisphere for both temperature and neutral wind components. The zonal wind and meridional wind perturbations also exhibited a smaller peak at low latitudes in the winter hemisphere and at the equator, respectively.

It is known that nonlinear interactions between planetary scale waves can contribute to atmospheric variability. For example, Thermosphere Ionosphere and Mesosphere Electric Dynamics (TIMED) satellite temperature observations during January 2005 showed that the nonlinear interactions between the W3 and the migrating diurnal tide could produce an eastward QTDW with zonal wavenumber 2 [*Palo et al.*, 2007]. The nonlinear interactions between the quasi-stationary planetary waves (QSPW) and the migrating tides lead to changes in tides, which then transmit the QSPW signals into the ionosphere at low and middle latitudes through the E region wind dynamo [*Liu et al.*, 2010; *Liu and Richmond*, 2013]. Nevertheless, the nonlinear interactions between QTDW and other planetary waves have not been reported.

Rapid growth of QSPWs and their forcing are believed to be the main drivers of the sudden stratospheric warming (SSW) at high latitudes in the winter hemisphere [*Matsuno*, 1971], which causes inter-hemispheric connections at different altitudes [e.g. *Karlsson et al.*, 2007, 2009; *Tan et al.*, 2012]. The wave-mean flow interactions could decelerate or even reverse the eastward winter stratospheric jet, which, in return, prevents the further growth of the QSPW. The SSW in the northern hemisphere occurs usually in January/February, accompanied with a strong zonal wavenumber 1 or 2 QSPW at high latitudes [*Pancheva et al.*, 2008; *Harada et al.*, 2009; *Manney et al.*, 2009; *Funke et al.*, 2010]. There have been recent studies suggesting possible connection between QTDW and SSW [*McCormick et al.*, 2009; *Chandran et al.*, 2013]. However, it is not clear if this is because both QTDW and SSW tend to occur in mid to late January, or if the flow condition around SSW is more favorable for QTDW propagation and/or amplification. In this paper, we investigate the influence of SSW on QTDW using the National Center for Atmosphere Research (NCAR) TIME-GCM. The numerial experiments are described in section 2. Section 3 are the analysis results from the model simulations. Section 4 discusses the contributions of QTDW to the summer mesospheric polar warming. Our conclusions are presented in section 5.

2. Datasets and analysis

2.1 TIMED satellite observations

The TIMED satellite was launched at the end of 2001, which focuses on the dynamics study of the mesosphere and lower thermosphere. The TIMED Doppler Imager (TIDI) instrument on board the TIMED satellite has been providing global horizontal wind observations since late January 2002. The NCAR-processed version 0307A of P9 line TIDI wind datasets are utilized here to investigate the inter-annual variations of the QTDWs during austral summer periods. The vertical resolution of the TIDI winds between 85 and 105 km is ~2 km, with the highest precision at ~95 km [*Killeen et al.*, 2006]. The version 0307A TIDI horizontal winds have been used in the study of mesospheric tidal variations and QTDWs [*Wu et al.*, 2008; *Gu et al.*, 2013]. A two-dimensional least square fitting method, which was provided by *Gu et al*. [2013a; 2015], is also adopted to extract the QTDW signals in this study.

2.2 TIME-GCM simulations

The NCAR TIME-GCM simulates the global atmosphere from the upper stratosphere to the thermosphere, and the ionospheric electrodynamics [*Roble and Ridley*, 1994; *Roble*, 2000; *Richmond et al.*, 1992], which is self consistent. The input solar EUV and UV spectral fluxes are parameterized by the solar flux index at 10.7 cm wavelength (F10.7), and it is set to 150 sfu (solar flux unit) in our model simulations. The auroral electron precipitation is parameterized by hemispheric power [*Roble and Ridley*, 1987] and the ionospheric convection is driven by the magnetosphere-ionosphere current system [Heelis *et al.*, 1982]. The hemispheric power is set to 16 and the cross-cap potential is set to 60 in our simulations. The gravity wave forcing is parameterized based on linear saturation theory [*Lindzen*, 1981]. Climatologic migrating tides from the Global Scale Wave Model (GSWM) are specified at the lower boundary. The model is capable of simulating the upward propagation of planetary waves by superimposing periodical geopotential height perturbations at the lower boundary (~30 km). We use the regular horizontal resolution of $5°\times5°$ longitude and latitude grids in the current study. There are 49 pressure levels from 10 hPa (~30 km) to the upper boundary of 3.5×10^{-10} hPa (~550 km) with a vertical resolution of one-half scale height. The tides are generally weak compared with climatology in this single version of TIME-GCM. But this does not alter our conclusion with regard to 2-day waves.

To simulate the QTDW, geopotential height perturbations of 1000 m with wavenumber 3 were forced at the TIME-GCM lower boundary. The Gaussian-shaped geopotential height perturbations for W3 peaked at 30°N, extending from 10°S to 70°N. To simulate the SSW, geopotential height perturbations of 1000 and 2800 m for a stationary planetary wave with zonal wavenumber 1 (SPW1) were specified at the lower boundary for weak and strong warming, respectively. The Gaussian-shaped geopotential height perturbations for SPW1 peaked at 60°N, extending from 35°N to 85°N. In fact, the European Centre for Medium-Range Weather Forecasts (ECMWF) dataset during 2011/2012 austral summer period shows that both the geopotential perturbations of the W3 and SPW1 maximize in the northern (winter) hemisphere at the model lower boundary (not shown). The model was run under perpetual conditions for 40 days with the calendar date set to January 20. Both the W3 and SPW1 gained maximum amplitudes on day 10 with a Gaussian-shaped increase from day 1 to 10. The forcing of W3 was reduced following the same Gaussian function from days 25 to 40. The forcing of SPW1 was sustained from days 10 to 40. The parameters for the control run (base case) and four different experimental runs (case 1, 2, 3, and 4) are summarized in Table 1. No W3 or SPW1 forcing was specified at the TIME-GCM lower boundary in the base case, which ran for 15 days to equilibrate and was utilized as initial conditions for the other experimental cases. Case 1 was a standard run for W3 and only geopotential height perturbations of W3 were forced. Case 2 and case 3 were designed to study the amplification of W3 under weak and strong SSW conditions, respectively. The same W3 forcing was added in cases 2 and 3, whereas the SPW1 forcing was stronger in case 3 than that in case 2. Case 4 was a standard run for SSW in which only the forcing of SPW1 was included.

3. Observational results

Figure 1 shows the ECMWF zonal mean temperature at 80N and 10 hPa from December to February during 2003-2012. The strongest SSW occurred in January 2009, followed by the second strongest SSW in January 2006. Besides, the SSWs in 2012, 2004 and 2010 were also very strong. Figure 2 shows the temporal variations of the wave number 3 QTDW in January and February during 2003-2012. The amplitudes were averaged between 90 and 100 km. The W3 peaked regularly in late January and early February every year but with strong inter-annual variabilities. For example, the W3 reached minima in January of 2008 and 2009. It is also clear that the W3 was strong during the strong SSW years of 2004, 2006 and 2012. Nevertheless, the W3 was extremely weak during the strongest SSW year of 2009. Figure 3 shows the averaged amplitudes of the wave number 2 QTDW between 90 and 100 km during 2003-2012, which also maximized in January and February. The W2 was the strongest during the strong SSW year of 2006, followed by the W2 event in 2012. We can see that the QTDWs could be very strong during some SSW years, but not during all the SSW years. Our question is whether the SSW and QTDW (both W2 and W3) impact each other, and this will be numerically studied in the following section.

4. Simulation results and Discussion

4.1 Zonal mean background condition

Since the model time was set perpetually on January 20, the background temperature and zonal wind in our simulations should show typical northern winter/southern summer conditions. Figures 4a and 4b show the zonal mean temperature and zonal mean zonal wind on model day 28 (when W3 peaks) in case 1, which only has W3 forcing. The zonal mean temperature in TIME-GCM shows a cold summer mesopause and a warm winter mesopause. In the upper stratosphere and mesosphere, the zonal mean zonal wind is easterly in the summer hemisphere and westerly in the winter hemisphere. It is clear that the global structures of the zonal mean temperature and zonal wind generally agree with climatology from for example previous TIMED/SABER temperature [*Mertens et al.*, 2009] and UARS/HRDI wind [*Swinbank and Ortland*, 2003] observations, as well as the NOGAPS-ALPHA forecast assimilations [*McCormack*, 2009].

We then investigate the atmospheric responses to the weak and strong SSW event in cases 2 and 3, respectively. Figures 4c and 4e show the temperature differences on model day 28 between case 2 and case 1, and between case 3 and case 1, respectively. In cases 1, 2 and 3, the same W3 forcing is specified at the lower boundary, whereas SPW1 is only specified in cases 2 and 3. The SPW1 forcing in case 2 is weaker than that in case 3. Compared with case 1, which does not have a stationary planetary wave specified at the model lower boundary, the temperature of case 2 is warmer by 15-20 K below 60 km and is colder by 20-25 K between 60 and 110 km at high latitudes in the winter hemisphere. Both the cooling and warming in case 3 are stronger than in case 2 due to the stronger SPW1 in case 3. The warming and cooling in the stratosphere and mesosphere for the strong SSW are ~40 K and ~60 K, respectively. In addition, weaker warming is observed between 70 and 100 km in the middle and low latitude regions and above 80 km at high latitudes in the summer hemisphere. The corresponding zonal mean zonal wind differences are shown in Figure 4d and 4f. The zonal mean zonal wind decreases by ~30 m/s and ~70 m/s in the winter stratosphere and lower mesosphere in the weak (case 2) and strong (case 3) SSW events, respectively. It increases by ~30 m/s and ~50 m/s in the mesopause region in the weak and strong SSW events, respectively. Generally, the SSW features in our simulations (e.g. the increasing temperature and decreasing westerly in the winter stratosphere high latitude region) agree with previous reports [*Funke et al.*, 2010; *Yamashita et al.*, 2010; *Tan et al.*, 2012].

4.2 The influences on W3

Figure 5a shows the wavenumber-period spectrum of the meridional wind during days 25-30 of case 1. The meridional wind at ~90 km and 22.5°S is utilized in the analysis. The westward wavenumber 3 QTDW dominates the whole spectrum, with negligible signatures at other wavenumbers and periods. The spectra of zonal wind and temperature show similar W3 signatures as the meridional wind (not shown). Figure 5b shows the latitudinal and vertical structure of the W3 in meridional wind, which maximizes at low latitudes in the southern hemisphere mesopause region with an amplitude of ~60 m/s. Shown in Figure 5c is the structure of the W3 in zonal wind, which peaks at middle and low latitudes in both hemispheres with maximum amplitude nearly half of the peak meridional wind amplitude. The zonal wind peak of ~30 m/s in the summer (southern) hemisphere is slightly larger than that of ~20 m/s in the winter hemisphere, most likely due to the additional amplification by the baroclinic/barotropic instability of the summer easterly. Figure 5d shows the global structure of the W3 in temperature, which also peaks at middle latitudes. In the summer hemisphere, the temperature perturbations peak at ~105 km and ~80 km with amplitudes of ~7 K and ~8 K, respectively. In the winter hemisphere, the peak of the W3 at ~80 km is much weaker than that between 100 and 110 km. We should note that the rapid decay of W3 near the model lower boundary (~30 km) is an artifact near the model lower boundary. In all, the vertical and latitudinal structures of the 2-day wave in our simulations generally agree with the TIMED/SABER temperature and TIMED/TIDI observations [*Palo et al.*, 2007; *Gu et al.*, 2013].

Figure 6 shows the temporal variations of the W3 in meridional wind at ~90 km for case 1, case 2 and case 3. Note that the same perturbations for W3 were forced at the lower model boundary for all the three experimental runs. The W3 forcing was gradually increased from day 1 to 10, and was reduced after day 25 with constant amplitude between day 10 and 25. The perturbations of SPW1 in case 2 were nearly three times larger than case 3, both of which were sustained after day 10 with a Gaussian-shaped increase from day 1 to 10. The W3 in case 1 is the strongest with an amplitude of ~60 m/s (Figure 6a). The maximum amplitudes of the W3 in case 2 and case 3 are ~40 m/s and ~35 m/s (Figure 6b and 6c), respectively. It is evident that the amplitudes of the W3 are weakened during the SSW periods. In the following, we will examine possible causes of the QTDW decrease during SSW.

The refractive index *m* of a forced planetary wave is [*Andrews et al.*, 1987]:

$$m^2 = \frac{\bar{q}_\varphi}{a(\bar{u}-c)} - \frac{s^2}{(a\cos\varphi)^2} - \frac{f^2}{4N^2H^2}, \qquad (1)$$

where s, c, ū, a, φ, f, N, and H are the zonal wavenumber, phase speed, zonal mean zonal wind, earth radius, latitude, Coriolis parameter, Brunt-Väisälä frequency, and scale height, respectively. Besides, $\bar{q}_\varphi$ is the latitudinal gradient of the quasi-geostrophic potential vorticity:

$$\bar{q}_\varphi = 2\Omega\cos\varphi - \left(\frac{(\bar{u}\cos\varphi)_\varphi}{a\cos\varphi}\right)_\varphi - \frac{a}{\rho}\left(\frac{f^2}{N^2}\rho\bar{u}_z\right)_z, \qquad (2)$$

where Ω is the angular speed of the earth's rotation, ρ is the background air density, and z means the vertical gradient. A necessary condition for baroclinic/barotropic instability is $\bar{q}_\varphi < 0$, and the planetary waves are propagating (evanescent) where m^2 is positive (negative). Moreover, the meridional and vertical components (EPY and EPZ) of the Eliassen-Palm (EP) flux vector (F) for planetary waves can also be calculated with reconstructed wave perturbations from the TIME-GCM, defined following *Andrews et al.* [1987] as:

$$\vec{F}_{EP} = \begin{bmatrix} \mathrm{EPY} \\ \mathrm{EPZ} \end{bmatrix} = \rho a\cos\varphi \begin{bmatrix} \dfrac{\bar{u}_z\overline{v'\theta'}}{\bar{\theta}_z} - \overline{v'u'} \\ \left[f - \dfrac{(\bar{u}\cos\varphi)_\varphi}{a\cos\varphi}\right]\dfrac{\overline{v'\theta'}}{\bar{\theta}_z} - \overline{w'u'} \end{bmatrix} \qquad (3)$$

Here u', v', w' and θ' are the QTDW perturbations in zonal wind, meridional wind, vertical wind and potential temperature, respectively.

First, we examine the baroclinic/barotropic instabilities, waveguide and the EP flux of the W3 for these cases. The averaged zonal mean zonal wind for case 1, case 2 and case 3 during days 25-30, when the W3 reaches the maximum amplitude, are depicted by the black contour lines in Figures 7a, 7c and 7e, respectively. Over-plotted are the negative regions of $\bar{q}_{\varphi}$ by blue shades, which is a prerequisite for the occurrence of mean flow instability, and the positive regions of the waveguide for W3 by orange shades, which show where wave progagation is favorable. Shown in Figures 7b, 7d and 7f are the EP flux vectors (red arrows) of W3 and their divergences (light blue shades and dot lines) for case 1, case 2 and case 3, respectively. We will first compare results of case 1 (Figures 7a and 7b) with case 2 (Figures 7c and 7d). A region of negative $\bar{q}_{\varphi}$ is seen in case 1 between 80 and 100 km at middle and high latitudes in the winter hemisphere, which are insignificant in case 2. This difference probably results from the different vertical shears in zonal wind between the two cases. Moreover, the region with negative $\bar{q}_{\varphi}$ in the summer stratosphere polar region is also slightly more extended in case 1. Correspondingly, the positive EP flux divergence for W3, which is an indication of wave source, is stronger in both the summer mesosphere polar region and the winter mesopause region for case 1. The positive EP flux divergence near the polar region of summer mesosphere is suggested to be evidence of wave amplification from the baroclinic/barotropic unstable region [*Liu et al.*, 2004]. The additional source for the W3 is evident from the positive EP flux divergence at the southward edge of the baroclinic/barotropic instability in the winter mesopause region for case 1 (Figure 7b).

Case 1 (Figures 7a and 7b) and case 3 (Figures 7e and 7f) are now compared. The stratospheric westerlies in the winter hemisphere polar region reverse to easterlies in case 3, which creates an area with negative $\bar{q}_\varphi$ in the winter polar mesosphere and stratopause, compared with case 1 (Figures 7a and 7e). Previous studies have found that planetary waves could be generated by the anomalous potential vorticity gradients in the winter middle atmospohere [*Zülicke and Becker*, 2013; *Sato and Nomoto*, 2015]. During SSW periods, the planetary wave signals are clearly indicated by the outflow of the EP flux vectors and positive EP flux divergences nearby the baroclinic/barotropic instabilities induced by the reversal of winter westerly [*Limpasuvan et al.*, 2012; *Chandran et al.*, 2013]. In our simulations, the additional W3 sources between 60°N and 90°N below 70 km in case 3 may be related to the nearby instability (Figures 7b and 7f), as found by *Liu et al.* [2004]. It is also seen that the summer easterly winds in case 3 are stronger than in case 2 and case 1, which results in a larger refractive index for the propagation of W3. The EP flux vectors in all the experimental runs show that the W3 propagates mainly southward from the northern hemisphere wave source region at lower altitudes, and then propagates upward after reaching the southern hemisphere. These propagation features agree well with previous model simulations [*Chang et al.*, 2011; *Yue et al.*, 2012].

The meridional and vertical components of the W3 EP flux (EPY and EPZ) are shown in Figure 8. It is clear that both the EPY and EPZ are the strongest in case 1, which is probably due to the energy transfer to child waves during the nonlinear interaction between W3 and SPW1 for cases 2 and 3. In the northern (winter) hemisphere, the stronger EPY and EPZ in case 1 may also be induced by the additional northern mesospheric barotropic/baroclinic instabilities (shown in Figure 7a), which is not found in case 2 and case 3. The EPY components for all three cases indicate southward propagation at lower altitudes from the wave source region in the winter hemisphere, and then northward propagation in the summer polar mesosphere near the region of instability. The EPZ mostly propagates upward, and is the strongest at middle and low latitudes in the summer hemisphere and much weaker in the winter hemisphere. This is in general agreement with the waveguide shown in Figure 7. Strong upward EPZ at ~30°N and ~100 km is only observed in case 1, which is probably related to the instability at middle and high latitudes (Figure 7a). Such instabilities and wave sources disappear in the SSW runs due to the deceleration or even reversal of the strong winter westerly winds.

Our simulations show that the instabilities at middle and high latitudes in the winter hemisphere mesopause region can also provide additional and significant sources for the amplification of W3 (case 1). Such instabilities and the corresponding sources for W3 are weakened during SSW periods due to the deceleration or even reversal of the winter stratospheric westerly winds. Our results also show that the summer easterlies in the stratosphere and lower mesosphere are strengthened during SSW periods, which results in larger waveguide and thus more favorable background condition for the propagation of W3. The fact that W3 becomes weaker in the presence of more favorable propagation conditions (and with the same wave source) in the summer hemisphere again suggests a loss of W3 wave energy. In the following section, we argue that the wave energy is transferred to child waves from nonlinear interaction of W3 with SPW1, namely the QTDW W2 component.

4.3 Nonlinear interaction between W3 and SPW1

Figure 9a shows the wavenumber-period spectrum of the meridional wind during model days 15-20 in case 3 at 100 km and 2.5 °N. A westward wavenumber 2 QTDW dominates the spectrum, which is different from the wavenumber 3 QTDW signature shown in Figure 5a. The spectra of other components, e.g., zonal wind and temperature, also show evident wavenumber 2 QTDW signatures. We should emphasize that W3 and SPW1 are the only planetary waves specified at the lower boundary of the TIME-GCM and no W2 signals are detected in the TIME-GCM runs with only W3 or SPW1 perturbations imposed at the lower boundary (case 1 and case 4). Thus, the W2 in case 2 and case 3 is generated by the nonlinear interaction between W3 and SPW1. The nonlinear interactions between two planetary waves can generate two child waves with frequencies and zonal wavenumbers being the sum and difference of the two parent waves [*Teitelbaum and Vial*, 1991]. For the nonlinear interactions between W3 and SPW1, the frequencies (f, cycles per day) and zonal wavenumbers (s) of the parents waves are: (f, s) = (0.5, 3) and (0, 1). Note here positive (negative) s indicates a westward (eastward) propagating wave. Thus the child waves are: (f, s) = (0.5, 4) and (0.5, 2). However, the wavenumber 4 QTDW is not well resolved in our simulation due to its lower phase speed and larger dissipation rate.

Figure 9b shows the cross section of the W2 in meridional wind for case 3 during model days 15-20. It maximizes in the equatorial and low latitude regions at ~100 km with a maximum amplitude of ~50 m/s. Shown in Figure 9c is the structure of the W2 in zonal wind and it peaks at middle latitudes with an amplitude nearly half as strong as the meridional wind. Figure 9d shows the global structure of the W2 in temperature, which exhibits similar global distributions as zonal wind. The temperature perturbations show maximum amplitudes of ~10 K in both hemispheres at ~105 km, and secondary maxima at ~85km: ~7 K in the southern hemisphere and ~5 K in the northern hemisphere. Figures 10a and 10b show the temporal variations of the W2 in meridional wind at 100 km for case 2 and case 3, respectively. The perturbations of the W2 in case 2 are weaker than in case 3, with maximum meridional wind amplitudes of ~35 m/s and ~55 m/s, respectively. This increase in the W2 amplitude in case 3 is consistent with the nonlinear interaction mechanism since one of the parent waves (SPW1) is stronger in case 3, resulting in a stronger child wave.

The mean flow instabilities, the waveguide and the EP flux of W2 are also examined to study the wave propagation and amplification. Figures 11a and 11c show the zonal mean zonal wind during model days 15-20, when the W2 reaches the strongest amplitude, for case 2 and case 3, respectively. In the northern hemisphere of case 3, the winter westerly in the upper stratosphere and lower mesosphere reverses in the polar region (Figure 11c), resulting in weak instabilities in this region. Weak instabilities are also observed at high latitudes in the winter mesopause region for case 2. In the southern hemisphere, the summer easterly jet core at middle latitudes is stronger in case 3, which results in a larger waveguide and thus more favorable condition for the propagation of W2 [*Liu et al.*, 2004]. The mean flow instabilities in the summer polar region are similar between case 2 and case 3.

Figures 11b and 11d show the EP flux of W2 and its divergence for case 2 and case 3, respectively. The EP flux vectors show that W2 propagates in both summer and winter hemispheres with comparable strength, which accounts for the nearly symmetric global distribution of the wave perturbations (Figure 9). The propagation features of W2 are different from W3 on that the W3 is more favorable to propagate in the summer hemisphere (Figure 7). This is mainly due to the relatively larger phase speed of W2, which results in a wider latitudinal distribution of positive waveguide for W2 and makes W2 less vulnerable to dissipation and critical layer filtering when propagating upward in the winter hemisphere [*Salby and Callaghan*, 2001]. Positive EP flux divergence is seen between 60 and 80 km at middle and high latitudes of the summer hemisphere for both case 2 and case 3, which is probably due to the wave amplification by the nearby region of instability [*Liu et al.*, 2004]. In addition, large positive EP flux divergence regions are found at middle and high latitudes of the northern hemisphere between 50-100 km for both case 2 and case 3, which is an indication of wave source due to the nonlinear interaction between SPW1 and W3. In addition, the positive EP flux divergence of W3 between 30 °N and 60 °N below 80 km (Figure 11d) may be related to the negative $\bar{q}_\varphi$ in the winter polar stratosphere (Figure 11c). This also agrees with the SSW-generating planetary wave signals presented by previous studies [*Liu et al.*, 2004; *Limpasuvan et al.*, 2012; *Chandran et al.*, 2013]. Figure 12 shows the meridional and vertical components (EPY and EPZ) of the EP flux of W2 separately. Both the EPY and EPZ are stronger in case 3 than case 2, which is again consistent with the nonlinear interaction mechanism. The vertical component EPZ (Figures 12b and 12d) clearly shows that the W2 propagates upward nearly symmetrically in both summer and winter hemispheres.

Figures 13a and 13b show the EP fluxes of W3 and SPW1 during model days 15-20 in case 3. Strong upward propagating SPW1 from wave source region is seen at middle and high latitudes in the winter hemisphere. Meanwhile, the energy of W3 propagates mainly southward from the same wave source region. Thus the nonlinear coupling between SPW1 and W3 is most likely to occur at lower altitudes in the winter hemisphere near the wave source region. In addition, weaker W3 energy can also be identified at higher altitudes and at middle and low latitudes in the winter hemisphere, which, together with the SPW1 activities at the same region, could also contribute to the source of W2 through nonlinear coupling. These speculations are further investigated by calculating the nonlinear advection tendency between W3 and SPW1. The nonlinear advection tendency terms in the momentum equations, which have been utilized by *Chang et al.* [2011] in studying the nonlinear coupling between QTDW and tides, are of the form:

$$\vec{F}_{advection} = -\vec{V} \cdot \nabla\vec{V} = -\left\{ \frac{u}{a\cos\varphi}\frac{\partial}{\partial\lambda} + \frac{v}{a}\frac{\partial}{\partial\varphi} + w\frac{\partial}{\partial z} \right\} \begin{bmatrix} u \\ v \end{bmatrix}^T \qquad (4)$$

Where *u*, *v* and *w* are the zonal, meridional and vertical winds, *a*, *z*, φ and λ are the earth radius, altitude, latitude, and longitude. By decomposing wind components, including zonal, meridional and vertical winds, into the forms of $r \approx \bar{r} + r_1 + r_2$ ($\bar{r}$, r_1 and r_2 represent the zonal mean wind and the wind perturbations of the two planetary waves, respectively), the zonal and meridional components of the nonlinear coupling tendencies for two planetary waves are:

$$F_{nonlinear,y} = -\frac{1}{a\cos\varphi}\left(u_1\frac{\partial v_2}{\partial\lambda} + u_2\frac{\partial v_1}{\partial\lambda}\right) - \frac{1}{a}\left(v_1\frac{\partial v_2}{\partial\varphi} + v_2\frac{\partial v_1}{\partial\varphi}\right) - \left(w_1\frac{\partial v_2}{\partial z} + w_2\frac{\partial v_1}{\partial z}\right) \quad (5)$$

where $\bar{u}$, $\bar{v}$ and $\bar{w}$ are the zonal mean zonal, meridional and vertical winds, u_1 and u_2, v_1 and v_2, w_1 and w_2 are the zonal, meridional, vertical wind perturbations for two different planetary waves.

Figure 13c shows the amplitude of the meridional component of the nonlinear advection tendency between W3 and SPW1 (equation 5). The nonlinear coupling between W3 and SPW1 maximizes at lower altitudes in the northern hemisphere, which is not surprising since both the W3 and SPW1 perturbations are forced at the lower model boundary in the northern hemisphere. Correspondingly, a strong W2 source is present at lower altitudes in the northern hemisphere, which is also suggested by the positive EP flux divergence shown in Figure 11d. The large nonlinear advection value at the lower boundary is due to the large wave sources forced there to compensate for the unrealistic wave decay usually found near the model lower boundary. Although the amplitude of the advection tendency at the lower model boundary may be too large compared with the peak in the mesosphere, it is still likely that the nonlinear interaction between W3 and SPW1 at ~30-45 km in the winter hemisphere is strong, since climatologically the sources of W3 and SPW1 are found to maximize in the winter hemisphere at stratospheric heights. There is an additional region extending from 60 km to about 100 km at low to mid latitudes where the advection tendency term becomes significant (with a peak at ~70km). This is again consistent with the positive EP flux divergence in Figure 11d, and is likely due to the nonlinear coupling of W3 and SPW1.

5. Conclusions

The influence of the SSW on the QTDW was investigated with NCAR TIME-GCM simulations. The westward wavenumber 3 QTDW was simulated by specifying geopotential height perturbations of 1000 m at the lower model boundary (~30 km) for both the standard W3 run and the SSW runs. Wavenumber 1 stationary planetary waves with geopotential height perturbations of 1000 m and 2800 m were forced in the northern hemisphere at the lower model boundary to induce minor and major SSWs, respectively.

We find that the mean flow instabilities at middle and high latitudes in the winter mesopause region can provide additional and essential sources for the amplification of W3, whereas such instabilities are weakened during SSW periods due to the deceleration or even reversal of the winter westerlies. The mean flow instabilities in the winter stratosphere polar region, induced by the mean wind reversal from westerly to easterly during SSW periods may also contribute to the amplification of W3. The waveguide of the W3 is larger during SSW periods, which favors the propagation of W3. The wave energy of W3 could be transmitted to child waves through the nonlinear interaction between W3 and stationary planetary waves during the SSW periods.

The nonlinear interaction between W3 and the SPW1 results in a new kind of westward QTDW with zonal wavenumber 2. The W2 is generated mainly in the wave source region, and then propagates into both summer and winter hemispheres. The meridional wind perturbations of W2 maximize in the equatorial region, whereas the zonal wind and temperature components peak at middle latitudes. The EP flux diagnostics show that W2 is capable of propagating in both hemispheres, which results in much more symmetric global structures than W3 for both wind and temperature components. This is probably due to the larger phase speed of W2, which results in larger latitudinal distributions of positive waveguide and makes W2 less vulnerable to dissipation and critical layer filtering by the background wind when propagating upward. In the summer hemisphere, the instabilities in the upper stratosphere and lower mesosphere polar region may contribute to the amplification of W2 through wave-mean flow interaction. In the winter hemisphere, the nonlinear coupling between W3 and SPW1 at middle and low latitudes between 50 km and 100 km, and the instabilities induced by the reversal of winter stratospheric westerly during SSW periods, most probably provide additional sources for W2. The stronger stationary planetary wave accounts for the stronger W2 perturbations during major SSW period by transmitting more energy to W2 during the nonlinear interaction between W3 and SPW1. Moreover, the background mean flow condition is also more favorable for the propagation of W2 during major SSW period with a larger waveguide.

We should note that the amplitudes of W3 and SPW1 specified at the lower boundary were both set to constant values in our simulation, while the wave sources would vary with time in real atmosphere. In addition, we utilized climatological state in January as the background condition in the simulation, which may be slightly different from the mean wind during specific years. For example, the SSWs generated in our simulation can only be classified as minor ones. Moreover, the TIMED observations (Figures 2 and 3) show that the W3 is usually much stronger than W2, even during strong SSW years of 2006 and 2009. Nevertheless, the W2 is even stronger than W3 in case 3. That is because the SPW1 forcing specified at the TIME-GCM lower boundary is stronger than observation to compensate the unrealistic wave dissipation at the lower boundary, which result in much stronger child wave of W2 during the nonlinear interaction. We also note that the W2 and W3 are both much stronger during the 2006 polar vortex displacement SSW event, but they are very weak during the 2009 vortex split SSW event. The different influence of the two types of SSW on QTDW also deserves our further investigation. In the future, the Whole Atmosphere Community Climate Model will be utilized to further study the influence of SSW on QTDWs under realistic atmospheric conditions, which may show new light on the variability of the QTDW and their possible correlations with SSW.

Acknowledgements

This work is funded by the Project Supported by the Specialized Research Fund for State Key Laboratories, the Project Funded by China Postdoctoral Science Foundation, the National Natural Science Foundation of China (41274150, 41421063), the Chinese Academy of Sciences Key Research Program (KZZD-EW-01-1), the National Basic Research Program of China (2012CB825605). HLL. acknowledges support from NSF grant AGS-1138784. The data utilized in this paper is from TIME-GCM simulations on NCAR Yellowstone computing system (ark:/85065/d7wd3xhc). The National Center for Atmospheric Research is sponsored by the National Science Foundation.

Reference

Andrews, D. G., J. R. Holton, and C. B. Leovy (1987), Middle Atmosphere Dynamics, 489 pp., Academic, San Diego, Calif.

Burks, D., and C. Leovy (1986), Planetary waves near the mesospheric easterly jet, *Geophys. Res. Lett., 13*, 193-196, doi: 10.1029/GL013i003p00193.

Chandran, A., R. R. Garcia, R. L. Collins, and L. C. Chang (2013), Secondary planetary waves in the middle and upper atmosphere following the stratospheric sudden warming event of January 2012, *Geophys. Res. Lett.*, *40*, 1861–1867, doi:10.1002/grl.50373.

Chang, L. C., S. E. Palo, and H. L. Liu (2011), Short-term variability in the migrating diurnal tide caused by interactions with the quasi 2 day wave, *J. Geophys. Res.*, *116*, D12112, doi:10.1029/2010JD014996.

Funke, B., M. López-Puertas, D. Bermejo-Pantaleón, M. García-Comas, G. P. Stiller, T. von Clarmann, M. Kiefer, and A. Linden (2010), Evidence for dynamical coupling from the lower atmosphere to the thermosphere during a major stratospheric warming, *Geophys. Res. Lett.*, *37*, L13803, doi:10.1029/2010GL043619.

Gu, S. Y., T. Li, X. K. Dou, Q. Wu, M. G. Mlynczak, and J. M. Russell (2013a), Observations of Quasi-Two-Day wave by TIMED/SABER and TIMED/TIDI, *J. Geophys. Res. Atmos.*, *118*, 1624–1639, doi:10.1002/jgrd.50191.

Gu, S. Y., T. Li, X. Dou, N.-N. Wang, D. Riggin, and D. Fritts (2013b), Long-term observations of the quasi two-day wave by Hawaii MF radar, *J. Geophys. Res.*

Space Physics, *118*, 7886–7894, doi:10.1002/2013JA018858.

Harada, Y., A. Goto, H. Hasegawa, N. Fujikawa, H. Naoe, and T. Hirooka (2009), A Major Stratospheric Sudden Warming Event in January 2009, *J. Atmos. Sci.*, *67*, 2052-2069, doi:http://dx.doi.org/10.1175/2009JAS3320.1.

Heelis, R. A., J. K.Lowell, and R. W.Spiro (1982), A model of the high-latitude ionsophere convection pattern, *J. Geophys. Res.*, *87*, 6339–6345.

Karlsson, B., H. Körnich, and J. Gumbel (2007), Evidence for interhemispheric stratosphere-mesosphere coupling derived from noctilucent cloud properties, *Geophys. Res. Lett.*, *34*, L16806, doi:10.1029/2007GL030282.

Karlsson, B., C. McLandress, and T. G. Shepherd (2009), Inter-hemispheric mesospheric coupling in a comprehensive middle atmosphere model, *J. Atmos. Sol. Terr. Phys.*, *71*, 518-530, doi:10.1016/j.jastp.2008.08.006.

Limpasuvan, V., and D. L. Wu (2009), Anomalous two-day wave behavior during the 2006 austral summer, *Geophys. Res. Lett.*, *36*, L04807, doi:10.1029/2008GL036387.

Limpasuvan, V., C. B. Leovy, and Y. J. Orsolini (2000), Observed temperature two-day wave and its relatives near the stratopause, *J. Atmos. Sci.*, *57*, 1689-1701, doi:10.1175/1520-0469(2000)057%3C1689:OTTDWA%3E2.0.CO;2.

Limpasuvan, V., J. H. Richter, Y. J. Orsolini, F. Stordal, and O.-K. Kvissel (2012), The roles of planetary and gravity waves during a major stratospheric sudden warming as characterized in WACCM, *Journal of Atmospheric and Solar-Terrestrial Physics, 78–79,* 84-98.

Lindzen, R. S. (1981), Turbulence and Stress Owing to Gravity Wave and Tidal Breakdown, *J. Geophys. Res.*, *86*, 9707-9714, doi:10.1029/JC086iC10p09707.

Liu, H. L., E. R. Talaat, R. G. Roble, R. S. Lieberman, D. M. Riggin, and J. H. Yee (2004), The 6.5-day wave and its seasonal variability in the middle and upper atmosphere, *J. Geophys. Res.*, *109*, D21112, doi:10.1029/2004JD004795.

Liu, H. L., and A. D. Richmond (2013), Attribution of ionospheric vertical plasma drift perturbations to large-scale waves and the dependence on solar activity, *J. Geophys. Res.*, *118*, 2452-2465, doi:10.1002/jgra.50265.

Liu, H. L., W. Wang, A. D. Richmond, and R. G. Roble (2010), Ionospheric variability due to planetary waves and tides for solar minimum conditions, *J. Geophys. Res.*, *115,* A00G01, doi:10.1029/2009JA015188.

Manney, G. L., et al. (2009), Satellite observations and modeling of transport in the upper troposphere through the lower mesosphere during the 2006 major stratospheric sudden warming, *Atmos Chem Phys*, *9*, 4775-4795, doi:10.5194/acp-9-4775-2009.

Matsuno, T. (1971), A Dynamical Model of the Stratospheric Sudden Warming, *J. Atmos. Sci.*, *28*, 1479-1494, doi:http://dx.doi.org/10.1175/1520-0469(1971)028<1479:ADMOTS>2.0.CO;2.

McCormack, J. P., L. Coy, and K. W. Hoppel (2009), Evolution of the quasi 2-day wave during January 2006, *J. Geophys. Res.*, *114*, D20115, doi:10.1029/2009JD012239.

Mertens, C. J., et al. (2009), Kinetic temperature and carbon dioxide from broadband infrared limb emission measurements taken from the TIMED/SABER instrument, *Adv. Space. Res.*, *43*, 15-27.

Palo, S. E., J. M. Forbes, X. Zhang, J. M. Russell, III, and M. G. Mlynczak (2007), An eastward propagating two-day wave: Evidence for nonlinear planetary wave and tidal coupling in the mesosphere and lower thermosphere, *Geophys. Res. Lett.*, *34*, L07807, doi:10.1029/2006GL027728.

Pancheva, D., et al. (2008), Latitudinal wave coupling of the stratosphere and mesosphere during the major stratospheric warming in 2003/2004, *Ann. Geophys.*, *26*, 467-483, doi:10.5194/angeo-26-467-2008.

Plumb, R. A. (1983), Baroclinic Instability of the Summer Mesosphere: A Mechanism for the Quasi-Two-Day Wave?, *J. Atmos. Sci.*, 40(1), 262-270, doi:10.1175/1520-0469(1983)040<0262:BIOTSM>2.0.CO;2.

Richmond, A. D., E. C. Ridley, and R. G. Roble (1992), A thermosphere/ionosphere general circulation model with coupled electrodynamics, *Geophys. Res. Lett.*, *19*, 601–604.

Riggin, D. M., R. S. Lieberman, R. A. Vincent, A. H. Manson, C. E. Meek, T. Nakamura, T. Tsuda, and Y. I. Portnyagin (2004), The 2-day wave during the boreal summer of 1994, *J. Geophys. Res.*, *109*, D08110, doi:10.1029/2003JD004493.

Roble, R. G. (2000), On the feasibility of developing a global atmospheric model extending from the ground to the exosphere, in *Atmospheric Science Across the Stratopause*, edited by D. E. Siskind, S. D. Eckermann, and M. E. Summers, 342 p., no. 123 in Geophysical Monograph Series, Americal Geophysical Union, Washington, D.C.

Roble, R. G., and E. C. Ridley (1987), An auroral model for the NCAR thermosphere general circulation model (TGCM), *Annales. Geophysicae.*, *5A*, 369–382.

Roble, R. G., and E. C. Ridley (1994), A thermosphere-ionosphere-mesosphere-electrodynamics general circulation model (time-GCM): Equinox solar cycle minimum simulations (30–500 km), *Geophys. Res. Lett.*, *21*, 417-420, doi:10.1029/93GL03391.

Rodgers, C. D., and A. J. Prata (1981), Evidence for a Traveling 2-Day Wave in the Middle Atmosphere, *J Geophys Res.*, *86,* 9661-9664, doi:10.1029/JC086iC10p09661.

Rojas, M., and W. Norton (2007), Amplification of the 2-day wave from mutual interaction of global Rossby-gravity and local modes in the summer mesosphere, *J. Geophys. Res.*, *112,* D12114, doi:10.1029/2006JD008084.

Salby, M. L. (1981), The 2-Day Wave in the Middle Atmosphere: Observations and Theory, *J. Geophys. Res.*, *86,* 9654-9660, doi:10.1029/JC086iC10p09654.

Salby, M. L., and P. F. Callaghan (2001), Seasonal Amplification of the 2-Day Wave: Relationship between Normal Mode and Instability, *J. Atmos. Sci.*, *58*(14), 1858-1869,

doi:10.1175/1520-0469(2001)058%3C1858:SAOTDW%3E2.0.CO;2.

Sato, K., and M. Nomoto (2015), Gravity Wave–Induced Anomalous Potential Vorticity Gradient Generating Planetary Waves in the Winter Mesosphere, *Journal of the Atmospheric Sciences*, *72*(9), 3609-3624.

Swinbank, R., and D. A. Ortland (2003), Compilation of wind data for the Upper Atmosphere Research Satellite (UARS) Reference Atmosphere Project, *J. Geophys. Res.*, *108*, 4615.

Tan, B., X. Chu, H.-L. Liu, C. Yamashita, and J. M. Russell, III (2012), Zonal-mean global teleconnection from 15 to 110 km derived from SABER and WACCM, *J. Geophys. Res.*, *117*, D10106, doi:10.1029/2011JD016750.

Teitelbaum, H., and F. Vial (1991), On Tidal Variability Induced by Nonlinear-Interaction with Planetary-Waves, *J Geophys Res.*, *96*, 14169-14178, doi:10.1029/91JA01019.

Tunbridge, V. M., D. J. Sandford, and N. J. Mitchell (2011), Zonal wave numbers of the summertime 2 day planetary wave observed in the mesosphere by EOS Aura Microwave Limb Sounder, *J. Geophys. Res.*, *116*, D11103, doi:10.1029/2010jd014567.

Wu, D. L., E. F. Fishbein, W. G. Read, and J. W. Waters (1996), Excitation and Evolution of the Quasi-2-Day Wave Observed in UARS/MLS Temperature Measurements, *Journal of the Atmospheric Sciences*, *53*, 728-738, doi:10.1175/1520-0469(1996)053<0728:EAEOTQ>2.0.CO;2.

Wu, D. L., P. B. Hays, W. R. Skinner, A. R. Marshall, M. D. Burrage, R. S. Lieberman, and D. A. Ortland (1993), Observations of the Quasi 2-Day Wave from the High-Resolution Doppler Imager on Uars, *Geophys. Res. Lett.*, *20*, 2853-2856, doi:10.1029/93GL03008.

Yamashita, C., H. -L. Liu, and X. Chu (2010), Responses of mesosphere and lower thermosphere temperatures to gravity wave forcing during stratospheric sudden warming, *Geophys. Res. Lett.*, 37, L09803, doi:10.1029/2009GL042351.

Yue, J., H.-L. Liu, and L. C. Chang (2012), Numerical investigation of the quasi 2 day wave in the mesosphere and lower thermosphere, *J. Geophys. Res.*, *117*, D05111, doi:10.1029/2011JD016574.

Zülicke, C., and E. Becker (2013), The structure of the mesosphere during sudden stratospheric warmings in a global circulation model, *Journal of Geophysical Research: Atmospheres*, *118*(5), 2255-2271.

	GP Height of W3	GP Height of SPW1
Base case	×	×
Case 1	1000 m	×
Case 2	1000 m	1000 m
Case 3	1000 m	2800 m
Case 4	×	2800 m

Table 1. The geopotential height perturbations of W3 and SPW1 specified at the lower model boundary for different model runs.

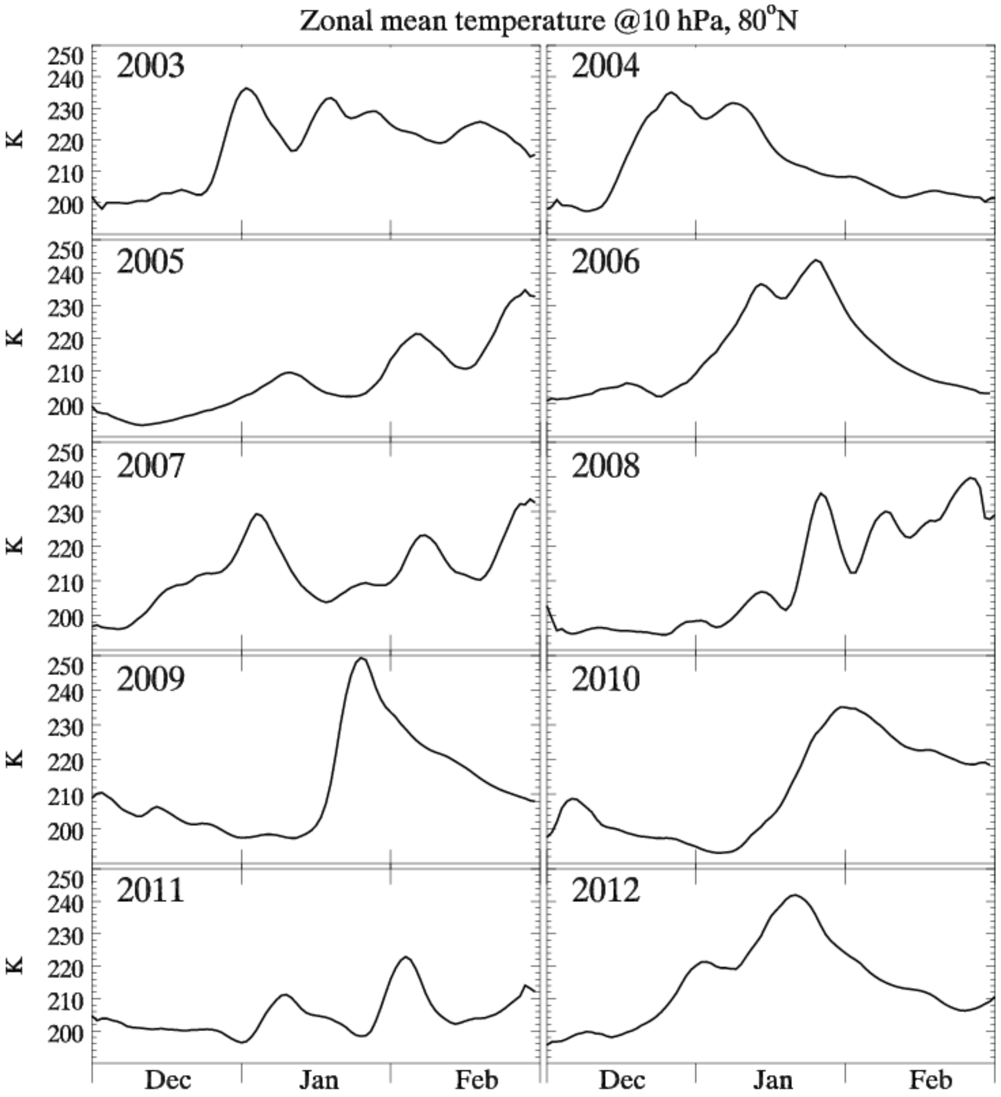

Figure 1. The ECMWF zonal mean temperature at 80 °N and 10 hPa from December to February during 2003-2012.

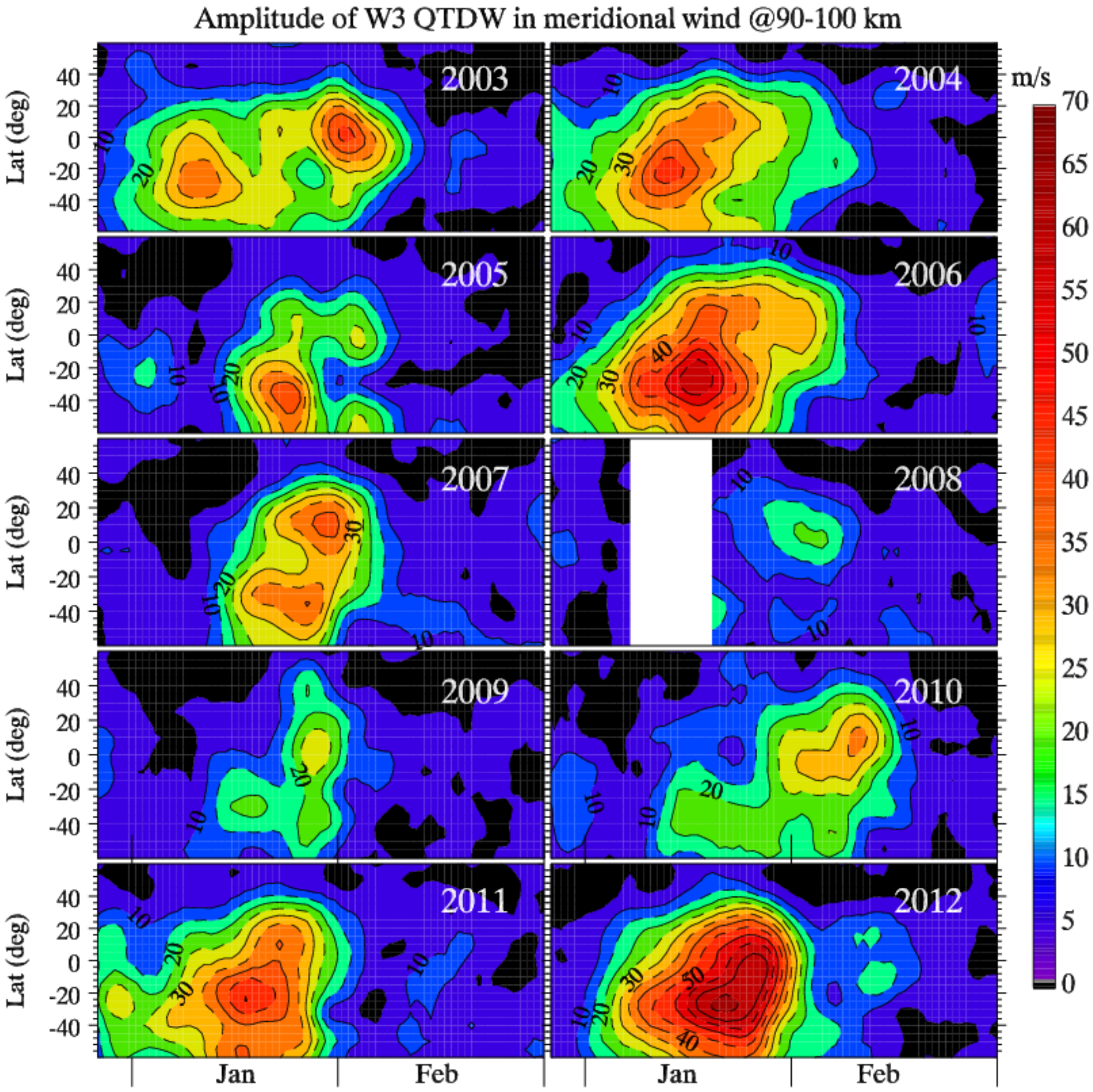

Figure 2. The temporal variations of the wave number 3 QTDW in January and February during 2003-2012. The amplitudes are averaged between 90 and 100 km.

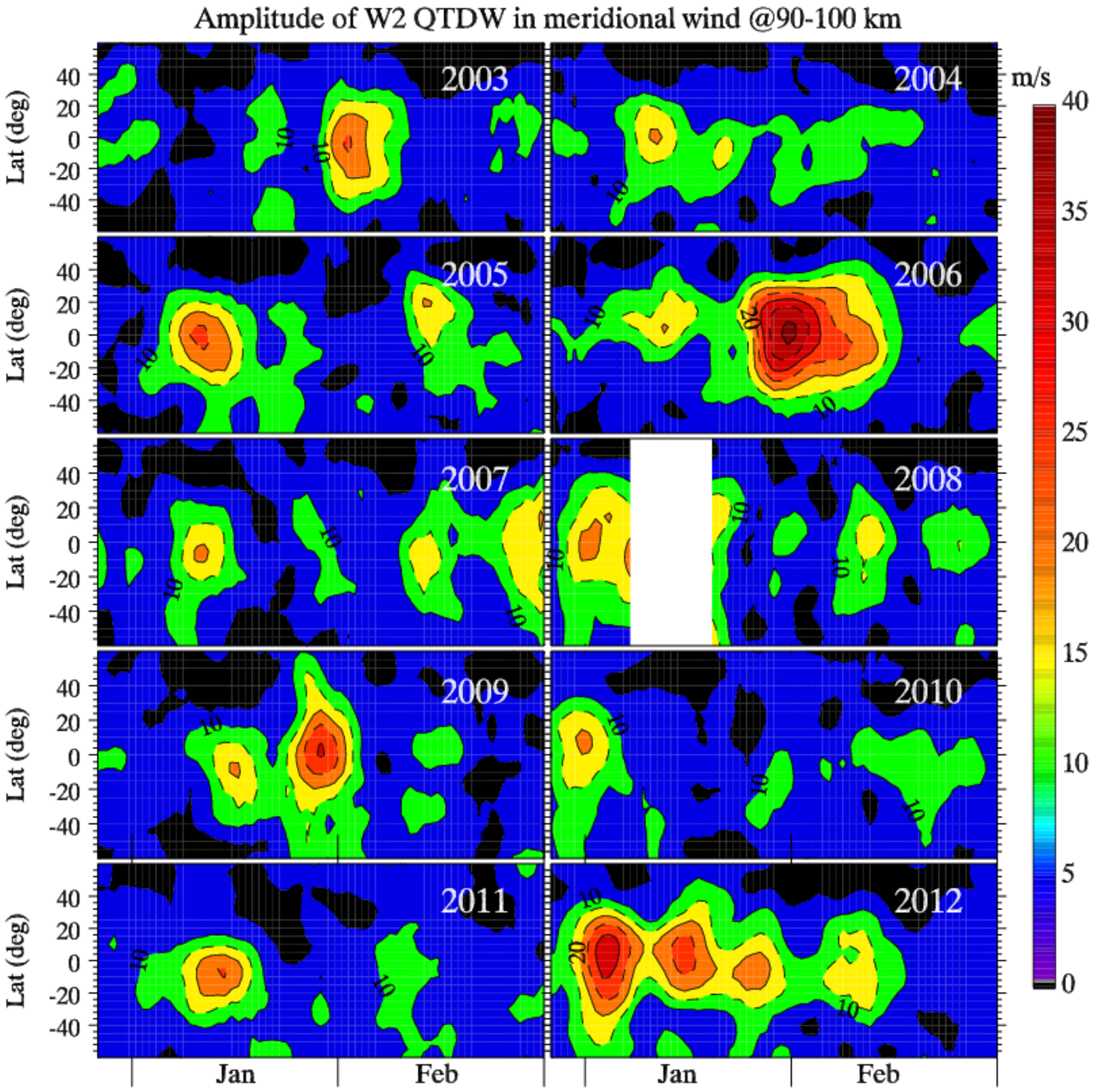

Figure 3. The same as Figure 2 but for the wave number 2 QTDW.

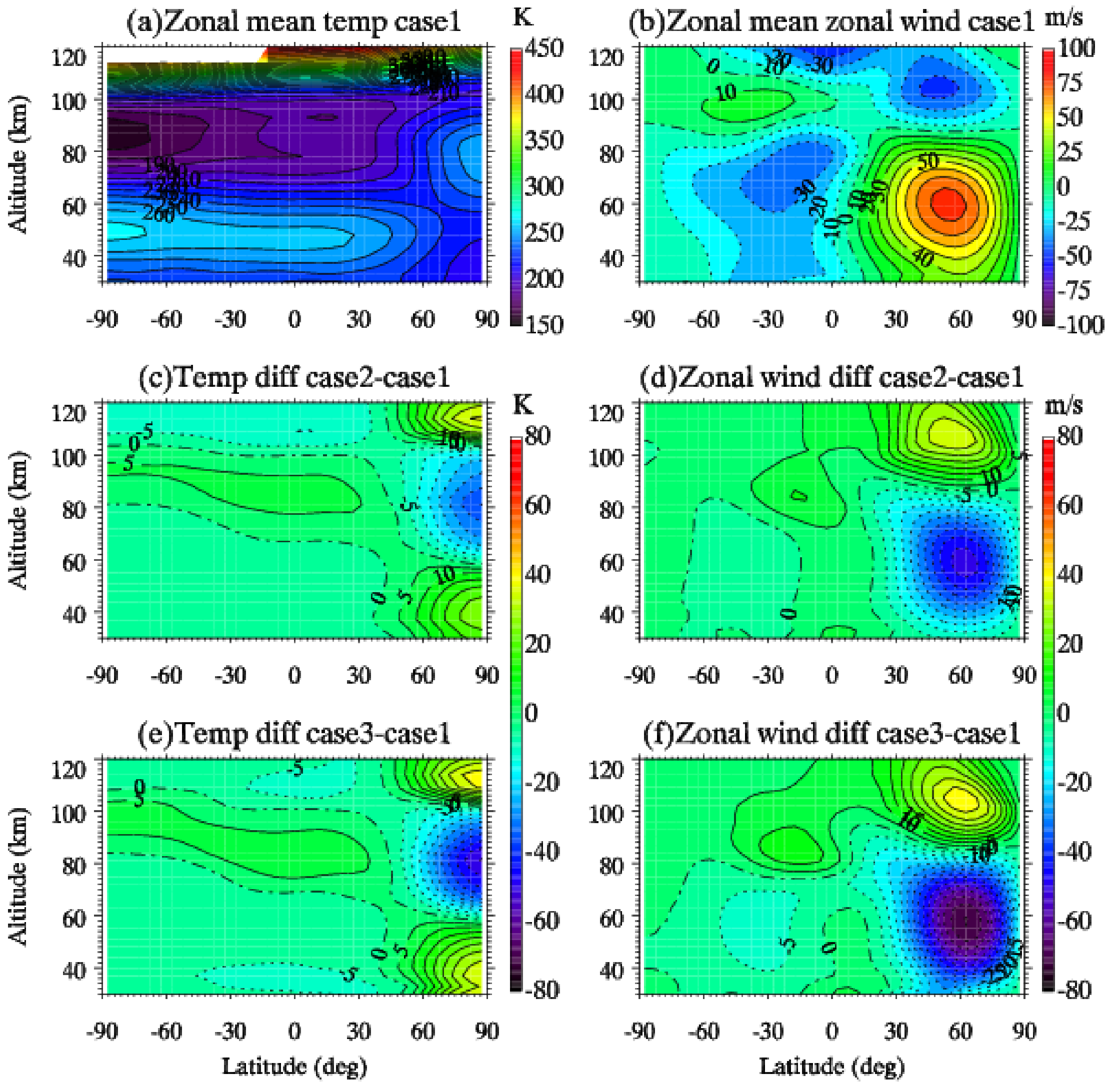

Figure 4. The zonal mean (a) temperature and (b) zonal wind in case 1 on model day 28. The temperature and zonal wind differences between (c, d) case 2 and case 1, (e, f) case 3 and case 1 are also shown. The temperature contour intervals are 10 K in (a) and 5 K in (c) and (e). The zonal wind contour intervals are 10 m/s in (b) and 5 m/s in (d) and (f).

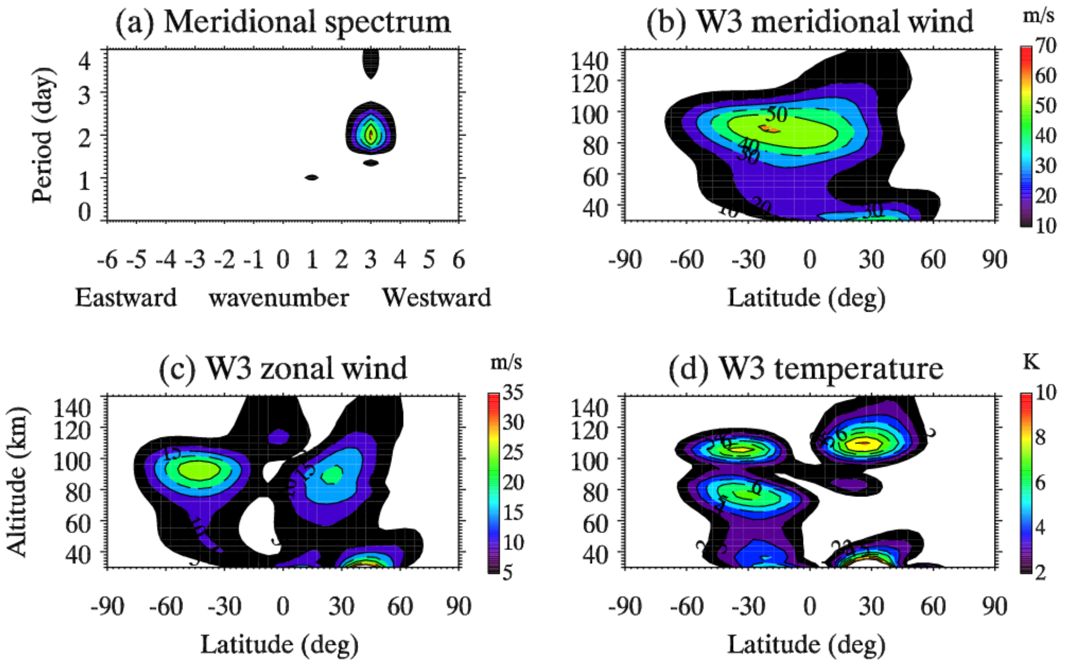

Figure 5. (a) The least-square fitting spectrum of the meridional wind at 22.5°S and ~90 km during model day 25-30 of case 1. A westward wave number 3 QTDW dominates the spectrum. The vertical and global structures of the W3 in meridional wind, zonal wind and temperature are shown in (b), (c) and (d), respectively. The contour intervals are 10 m/s, 5 m/s and 1 K for meridional wind, zonal wind and temperature, respectively.

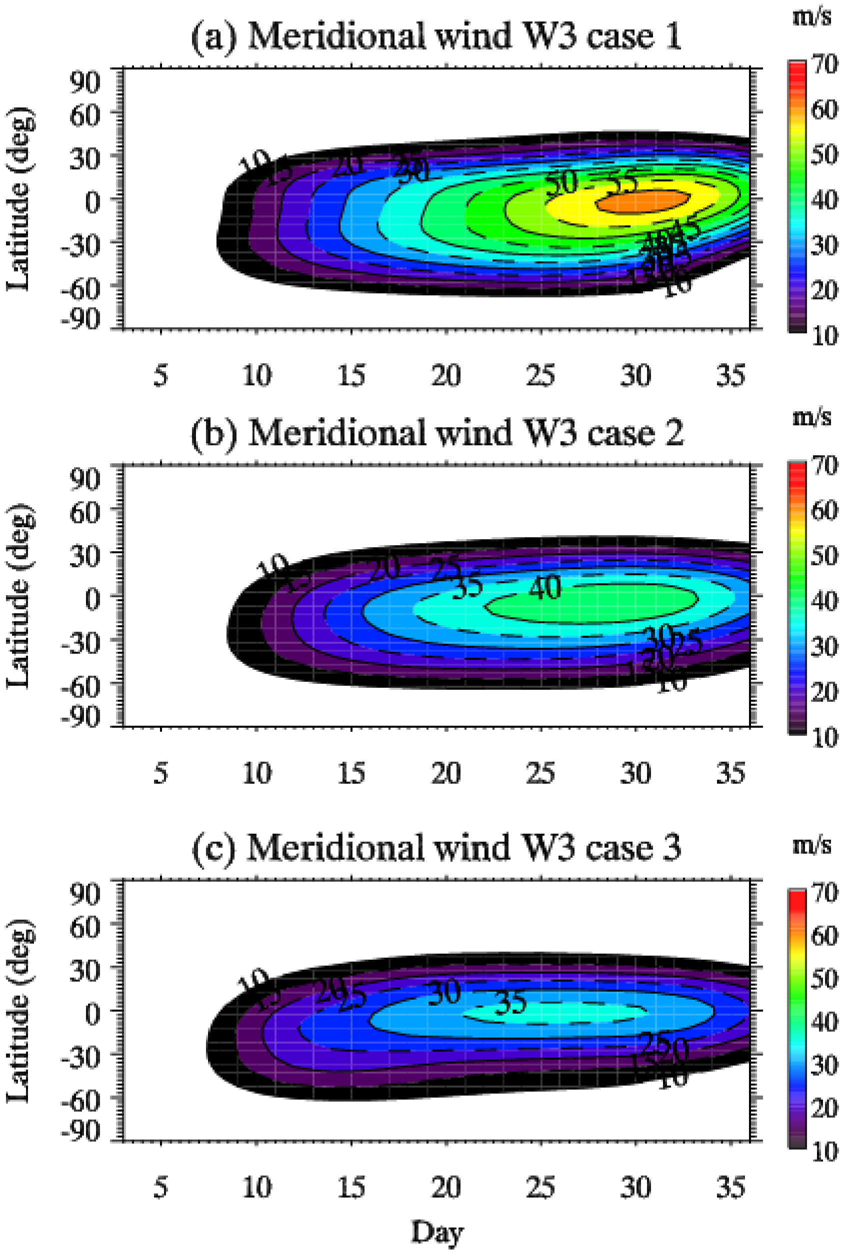

Figure 6. The temporal variations of the W3 at 90 km for (a) case 1, (b) case 2 and (c) case 3. Geopotential height perturbations of 1000 m are forced at the lower boundary for all the three control runs to simulate the W3. SPW1 geopotential height perturbations of 1000 m and 2800 m are forced at the lower boundary to induce the weak and strong SSWs in case 2 and case 3, respectively. No SPW1 perturbations are forced at the lower boundary of case 1. The contour intervals are 5 m/s.

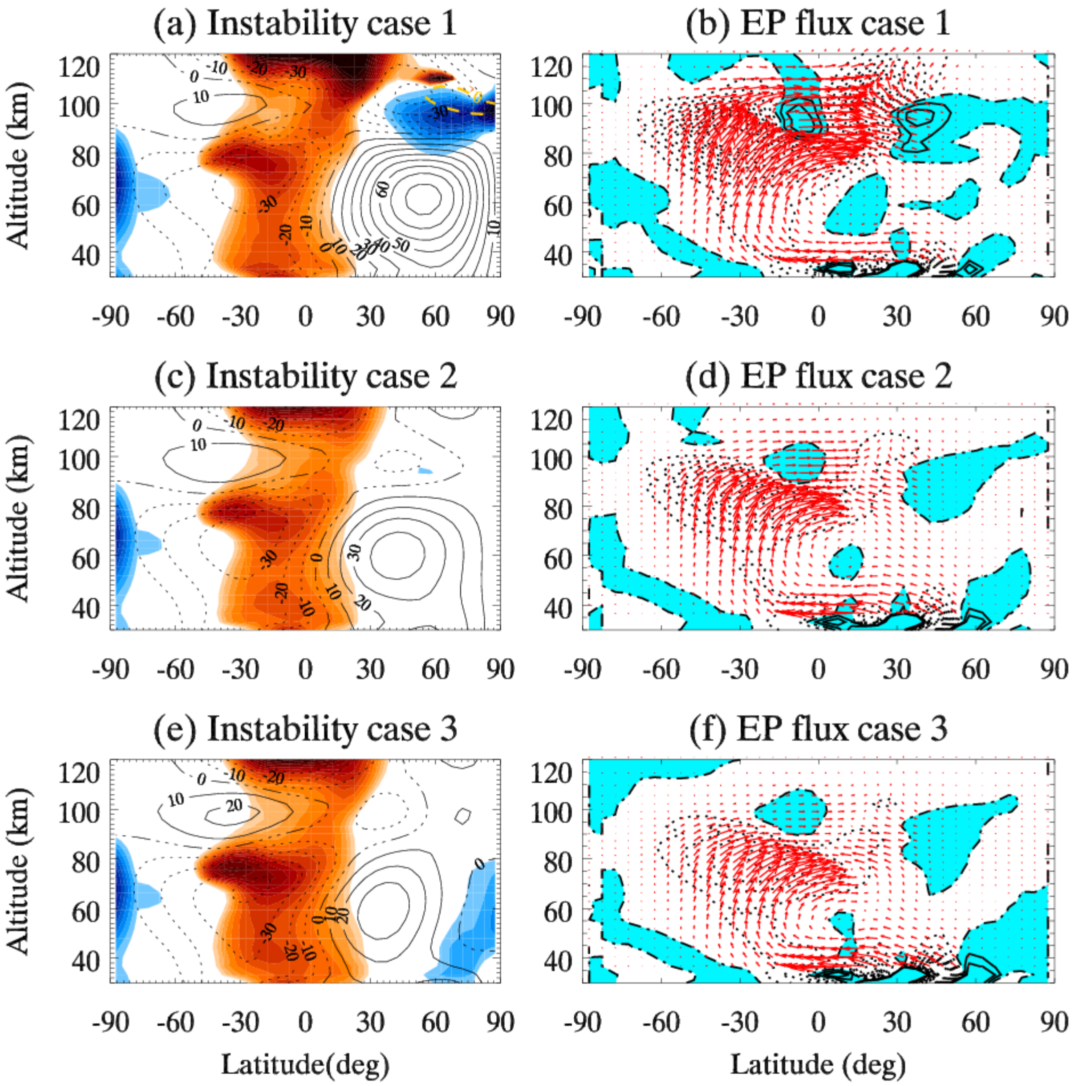

Figure 7. The zonal mean zonal wind during model days 25-30 for (a) case 1, (c) case 2 and (e) case 3. The baroclinic/barotropic instabilities are overplotted with blue shades. The orange shaded region denotes the positive (propagating) waveguide (m^2) for W3. Shown on the right are the EP flux vectors (red arrows) and their divergences (light blue shade for positive value, dot line for negative value) for (b) case 1, (d) case 2 and (f) case 3. The contour intervals for the EP flux divergence are 2 m/s/day.

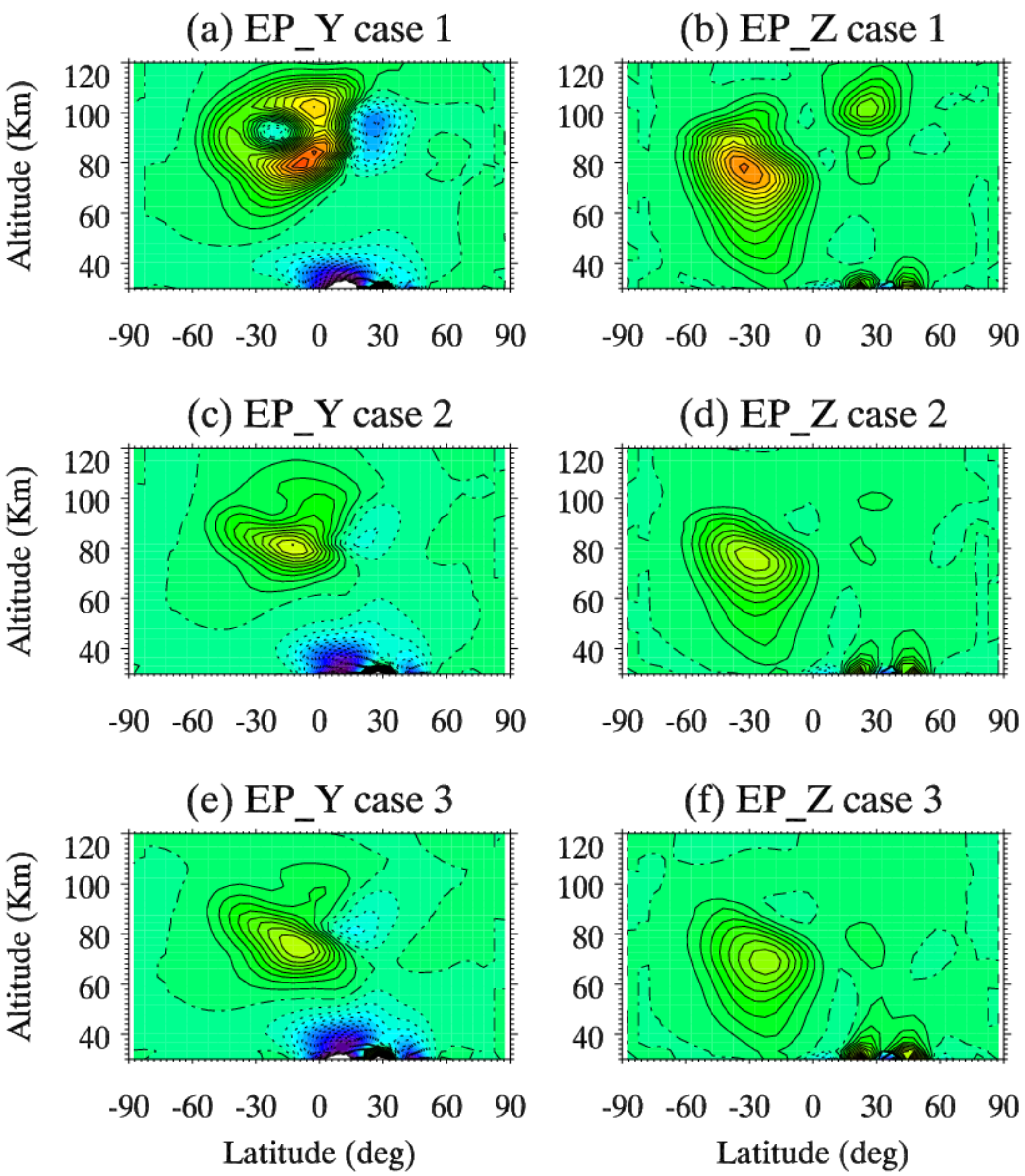

Figure 8. (left) Meridional and (right) vertical components of the EP flux of the W3 during model day 25-30 for (a, b) case 1, (c, d) case 2 and (e, f) case 3. The solid contours are for northward or upward directions. Both components have been normalized by the air density.

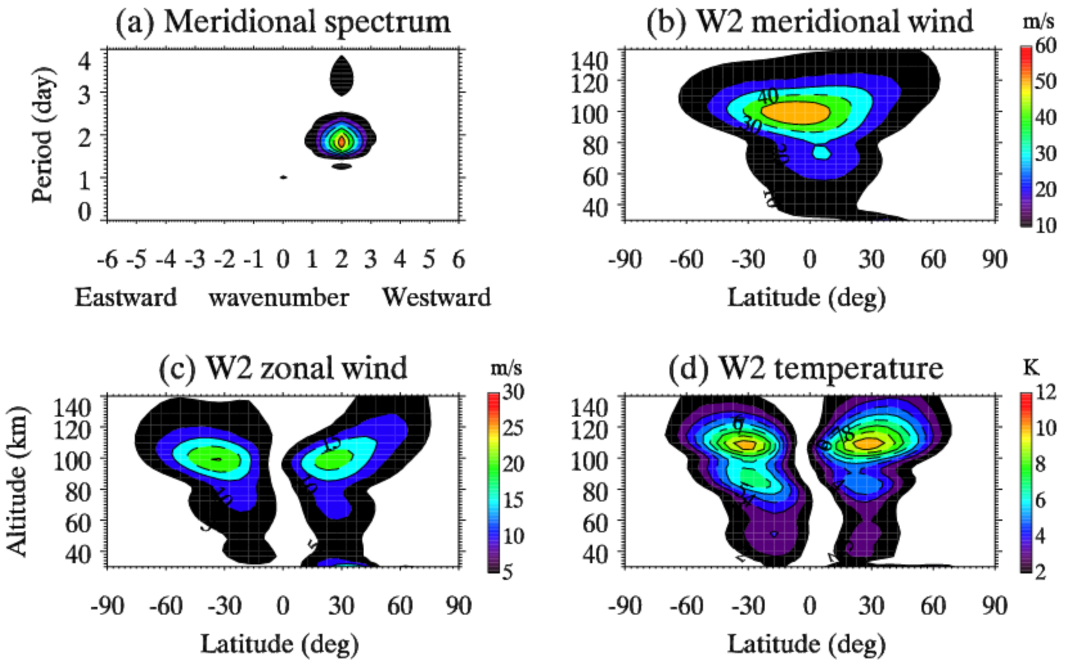

Figure 9. Similar to Figure 5 but for case 3 during model days 15-20. Figure 9a shows the meridional wind spectrum at 100 km and 2.5 °N. Figures 9b, 9c and 9d show the global and vertical structures of W2 for meridional wind, zonal wind and temperature, respectively.

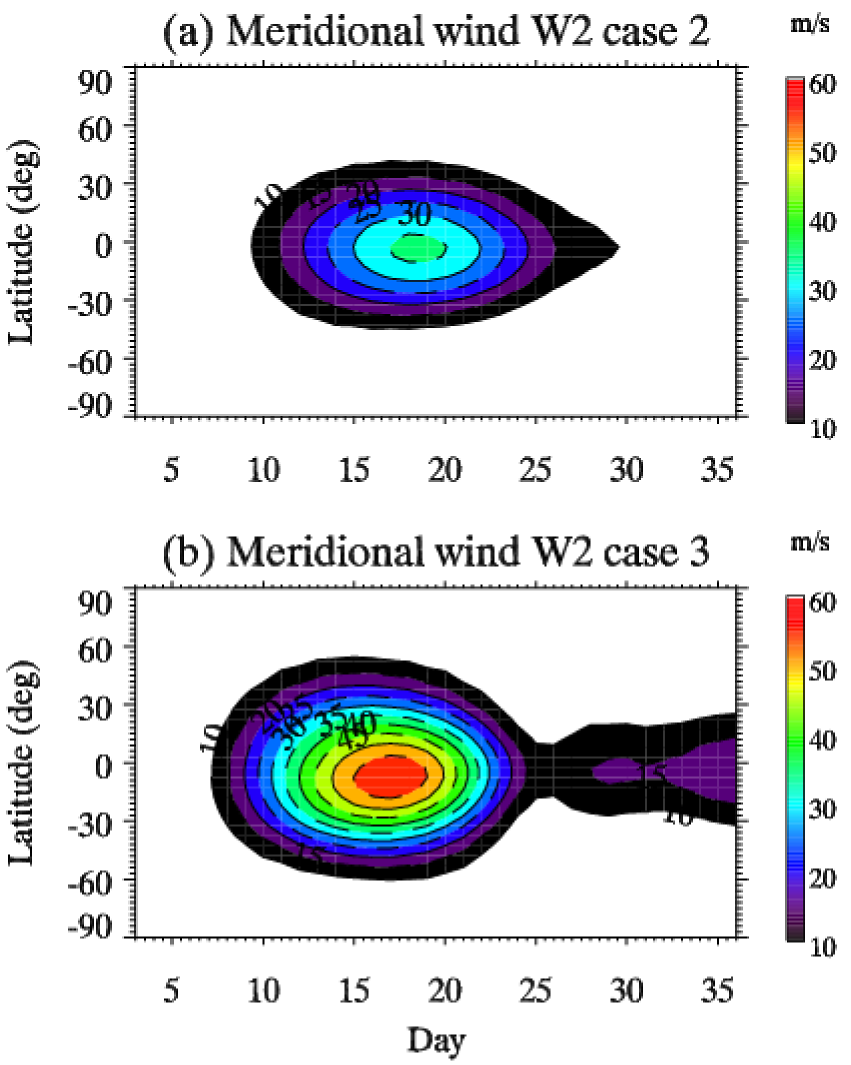

Figure 10. The temporal variaitions of the W2 at 100 km for (a) case 2 and (b) case 3. The contour intervals are 5 m/s.

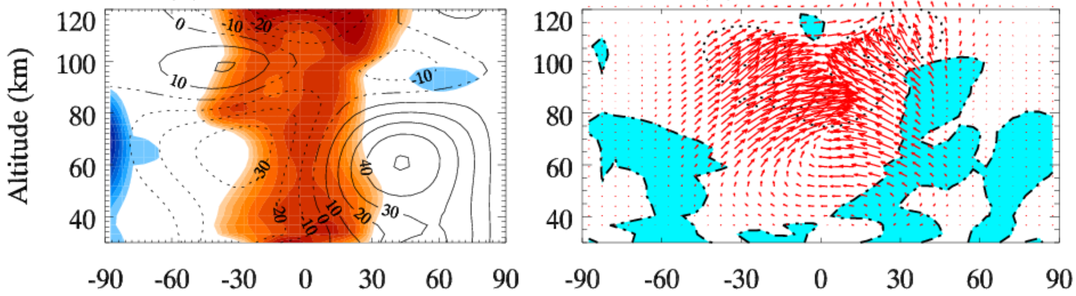
(a) Instability case 2

(b) EP flux case 2

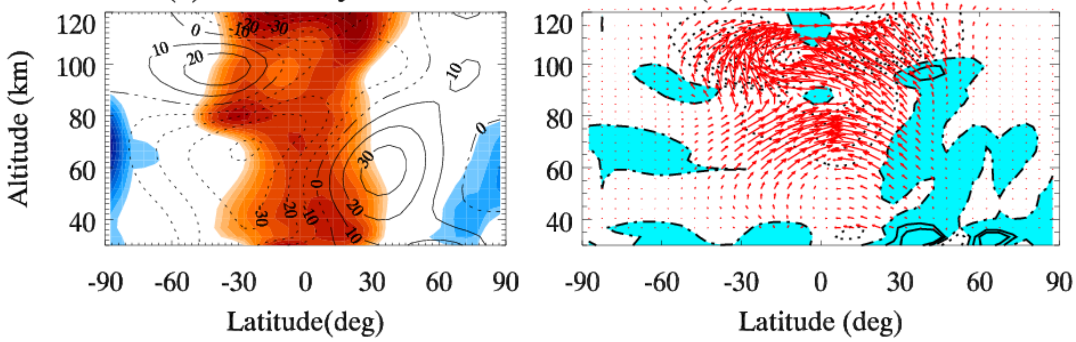
(c) Instability case 3

(d) EP flux case 3

Figure 11. The same as Figure 7 but for the W2 during model day 15-20 for (a, b) case 2 and (c, d) case 3.

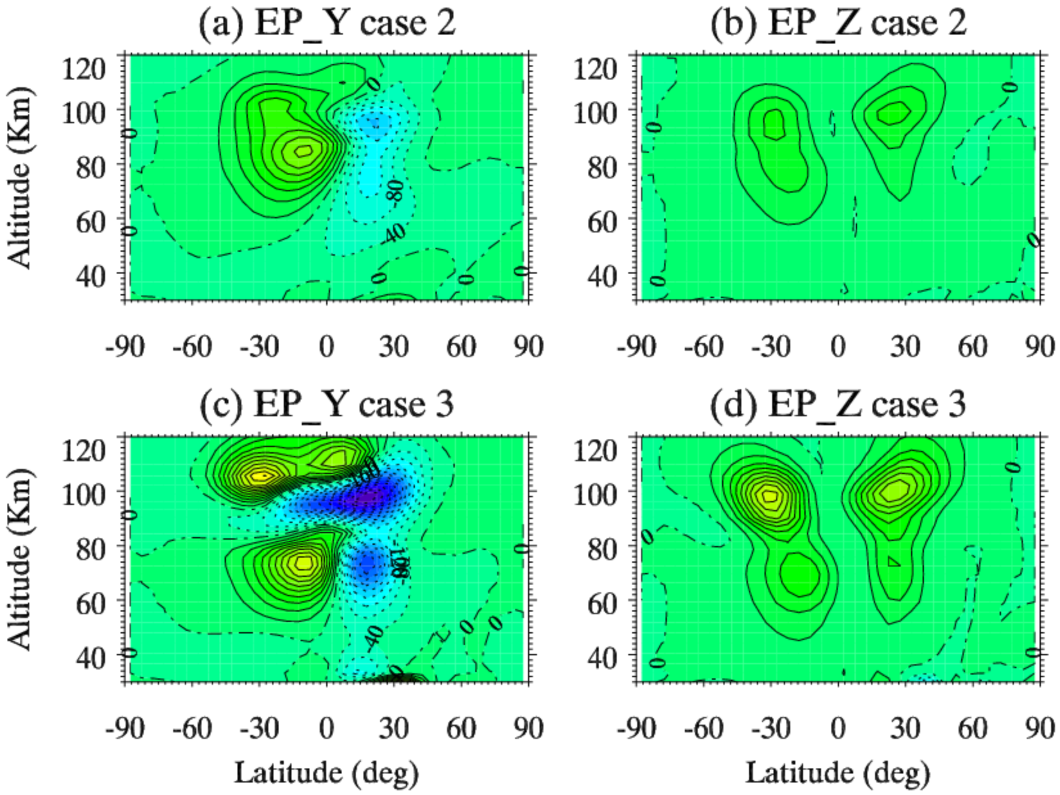

Figure 12. The same as Figure 8 but for the W2 during model day 15-20 for (a, b) case 2 and (c, d) case 3.

(a) SPW1 EP flux

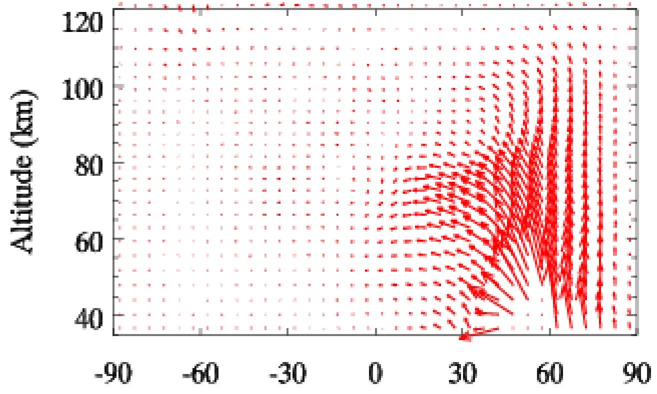

(b) W3 EP flux

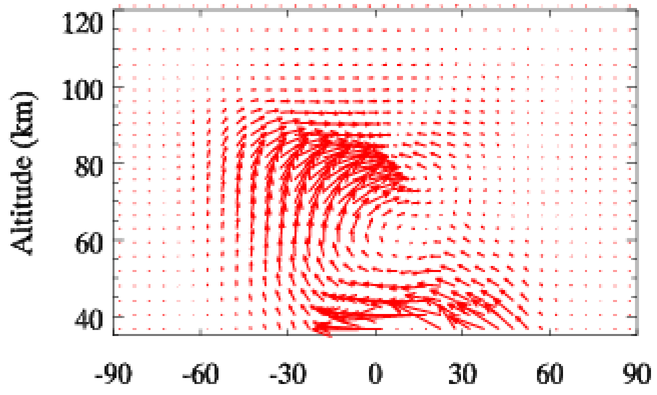

(c) Meridional nonlinear advection

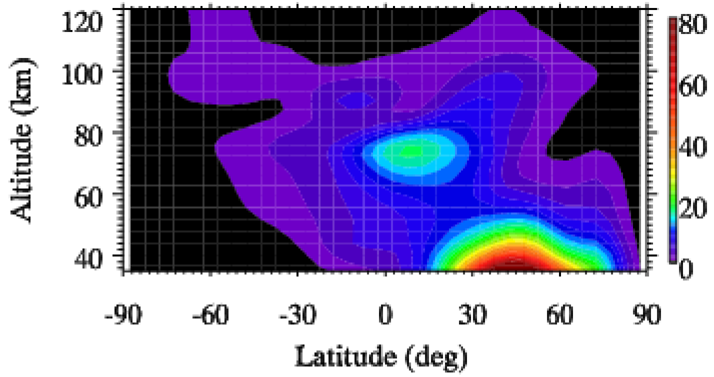

Figure 13. The EP flux vectors of (a) the SPW1 and (b) the W3 during model day 15-20 of case 3. (c) The amplitude (m/s^2) of the meridional component of the nonlinear advection tendency between W3 and SPW1.